

Deep-Learning Discovers Macroscopic Governing Equations for Viscous Gravity Currents from Microscopic Simulation Data

Junsheng Zeng¹, Hao Xu², Yuntian Chen¹, and Dongxiao Zhang^{3*}

AFFILIATIONS

¹ Frontier Research Center, Peng Cheng Laboratory, Shenzhen 518000, P. R. China

² College of Engineering, Peking University, Beijing 100871, P. R. China

³ School of Environmental Science and Engineering, Southern University of Science and
Technology, Shenzhen 518055, P. R. China

*Author to whom correspondence should be addressed: zhangdx@sustech.edu.cn

ABSTRACT

Although deep-learning has been successfully applied in a variety of science and engineering problems owing to its strong high-dimensional nonlinear mapping capability, it is of limited use in scientific knowledge discovery. In this work, we propose a deep-learning based framework to discover the macroscopic governing equation of viscous gravity current based on high-resolution microscopic simulation data without the need for prior knowledge of underlying terms. For two typical scenarios with different viscosity ratios, the deep-learning based equations exactly capture the same dominated terms as the theoretically derived equations for describing long-term asymptotic behaviors, which validates the proposed framework. Unknown macroscopic equations are then obtained for describing short-term behaviors, and hidden mechanisms are eventually discovered with deep-learned explainable compensation terms and corresponding coefficients. Consequently, the presented deep-learning framework shows considerable potential for discovering unrevealed intrinsic laws in scientific semantic space from raw experimental or simulation results in data space.

Deep-learning algorithms are currently being successfully applied in numerous science and engineering fields, such as physics,^{1,2} earth science,^{3,4} and computer vision and speech recognition.⁵ The advantage of deep-learning algorithms is their strong capability of constructing high-dimensional nonlinear mappings. Therefore, a deep-learning based surrogate model may be trained to effectively describe a physical process based on collected observation data. However, this type of surrogate model constitutes a “black box” with poor explainability, and fails to deepen our understanding of the essences of the physical process, which greatly decreases its utility. Considering the aforementioned issues, a salient question becomes: Does a machine learning approach exist that possesses both strong expressive capability and scientific explainability? Furthermore, is it possible to discover new scientific knowledge (e.g., macroscopic equations) from observations (e.g., microscopic simulation data), so that it can be well understood and conveniently applied in practice?

This constitutes a challenging problem, which combines knowledge discovery and explainable machine learning.⁶ The key to explainability for a machine learning based surrogate is to transform high-dimensional mapping from data space into semantic space, and obtain an intuitive and interpretable understanding about the mapping. In modern sciences, the most widely acceptable semantic form or knowledge expression form is represented by partial/ordinary differential equations (PDEs/ODEs), which are usually concise and easy-to-understand. To find the parsimonious PDEs hidden in data, recently, Xu et al.⁷ proposed a deep learning-genetic algorithm (DLGA) framework. In this framework, a deep neural network is utilized to calculate derivatives and generate meta-data, and the genetic algorithm is employed to discover the form of PDEs without the need of including the true terms in the initial guess. The deep neural network has been utilized in PDE discovery in previous works,^{8–10} because the derivatives calculated by automatic differentiation are more accurate and robust to noise. In the process of the genetic algorithm, genomes are composed of several basic genes, which can be adjusted according to the situation of the discovery process, which markedly increases both flexibility and practicability. Compared to other sparse regression methods, including LASSO,¹¹ SINDY,^{12,13} sequential threshold ridge regression (STRidge),^{14,15} and sparse Bayesian regression,¹⁶ the genetic algorithm does not need a complete candidate library beforehand,¹⁷ which may be impossible for many real-world applications. Meanwhile, the integral form is an efficient approach to facilitate the PDE discovery process and increase the accuracy of discovered PDEs.¹⁸

In this work, we attempt to employ the deep-learning based PDE discovery framework⁷ to discover unknown macroscopic equations for a real physical process, i.e., viscous gravity current. Viscous gravity current is an important natural phenomenon in geophysics,^{19–21} and typical scenarios include displacement flows in oil reservoirs,²² sea water intrusion,^{23,24} water injection in geothermal reservoirs,²⁵ pollutant dispersion through groundwater,²⁶ and proppant transport in hydraulic fractures.^{21,27} Essentially, viscous gravity current is a gravity-driven flow constrained in porous media or narrow vertical fractures due to the density difference between intruding and *in-situ* fluid, which forms a remarkable sharp interface at macro-scale, i.e., the current front. As a consequence, identification of a macroscopic equation for describing the evolution of current front height is a crucial issue. In extant literature, there exist many theoretically derived macroscopic equations for viscous gravity currents under various conditions, such as different viscosity ratio,¹⁹ multi-layer porous media,²⁸ non-Newtonian intruding fluid,^{29–31} and varying horizontal permeability.³² However, these works largely focus on long-term asymptotic behaviors of viscous gravity currents, and macroscopic equations for capturing short-term behaviors remain undetermined.

Different from previous works in data-driven PDE discovery, the training data of current front height are directly extracted from high-resolution microscopic simulation results instead of solving already-known model equations, and the long-term theoretical PDEs are only utilized in posterior tests as a reference. Consequently, no prior knowledge about the underlying equations is needed or utilized in the proposed method. By quantitatively comparing discovered PDEs with theoretical PDEs, the hidden mechanisms can be elucidated, which can be expressed as compensation terms for remedying the original theoretically derived PDEs to capture short-term behaviors in viscous gravity currents.

In this work, we consider a viscous gravity current process in a rectangle vertical fracture with non-penetration boundaries, as shown in Figure 1(a). The permeability and porosity of the fracture are considered as constant, and fluid leak-off, as well as other source terms, are ignored for simplicity. Then, the fluid motion in this 2D system is governed by the Darcy's equation $\vec{u} = -(k/\mu)(\nabla P - \rho \vec{g})$ and continuity equation $\nabla \cdot \vec{u} = 0$, where k is the permeability of fracture; ρ and μ are the fluid viscosity and density, respectively; P is the pressure gradient; \vec{g} is the gravity acceleration; and \vec{u} is the two-dimensional velocity of fluid. Then, determination of how the one-dimensional current front height $h(t, x)$ evolves at macro-scale, irrespective of specified two-dimensional pressure and velocity distributions, constitutes the primary aim.

Here, the observation data are extracted from 2D numerical simulation, also referred to as microscopic simulation. Fluid pressure is obtained by solving a Poisson equation, and the interface of the two phases are tracked with a conservative level-set method³³ (cf. Supplemental Materials, Section I). In this work, two typical scenarios of viscous gravity currents are investigated. For case I, viscosity of the heavy fluid is assumed to be equal to that of light fluid, i.e., $\mu_1 = \mu_2$; whereas, for case II, it is assumed that $\mu_1 \gg \mu_2$. For these two cases, the current front shape in long-term regimes are approximately linear and parabolic, respectively. By tracking the contour line of level set function $C = 0.5$ in the microscopic simulation results, the spatio-temporal evolving history of current front height is then obtained.

Without loss of generality, related variables, including front height h , horizontal location x , and time t , are normalized through non-dimensional analysis prior to subsequential deep-learning, and the dimensionless variables are defined as:

$$h^* = \frac{h}{H}; \quad x^* = \frac{x}{H}; \quad t^* = \frac{t\Delta\rho gk}{\mu_1 H} \quad (1)$$

where H is the total domain height; and $\Delta\rho$ is the density difference between the two fluids. It is worth noting that the obtained PDEs by deep-learning framework are indeed universal forms for similar processes if simulation data are nondimensionalized by equation (1) (cf. Supplemental Materials, Section II). In fact, if ignoring source/sink terms and inhomogeneity of vertical permeability, 1D macroscopic equations for all viscous gravity currents can be expressed in a unified conservative form, i.e., $\partial h^* / \partial t^* + \partial F^* / \partial x^* = 0$, where F^* indicates dimensionless flux. Then, for a to-be-investigated viscous gravity current process, the goal of discovering a concise PDE for front height evolution can be converted into a sparse regression problem of approximating flux F^* through basic algebraic combinations of height h^* and its arbitrary-order derivatives, such as $\partial h^* / \partial x^*$ and $\partial^2 h^* / \partial x^{*2}$. It is worth noting that, prior to regression, flux and derivatives should be calculated in advance based on raw training data. Particularly, flux F^* can be calculated through integration $F^*(t^*, x^*) = \int_{x_0^*}^{x^*} (-\partial h^* / \partial t^*) dx^*$.

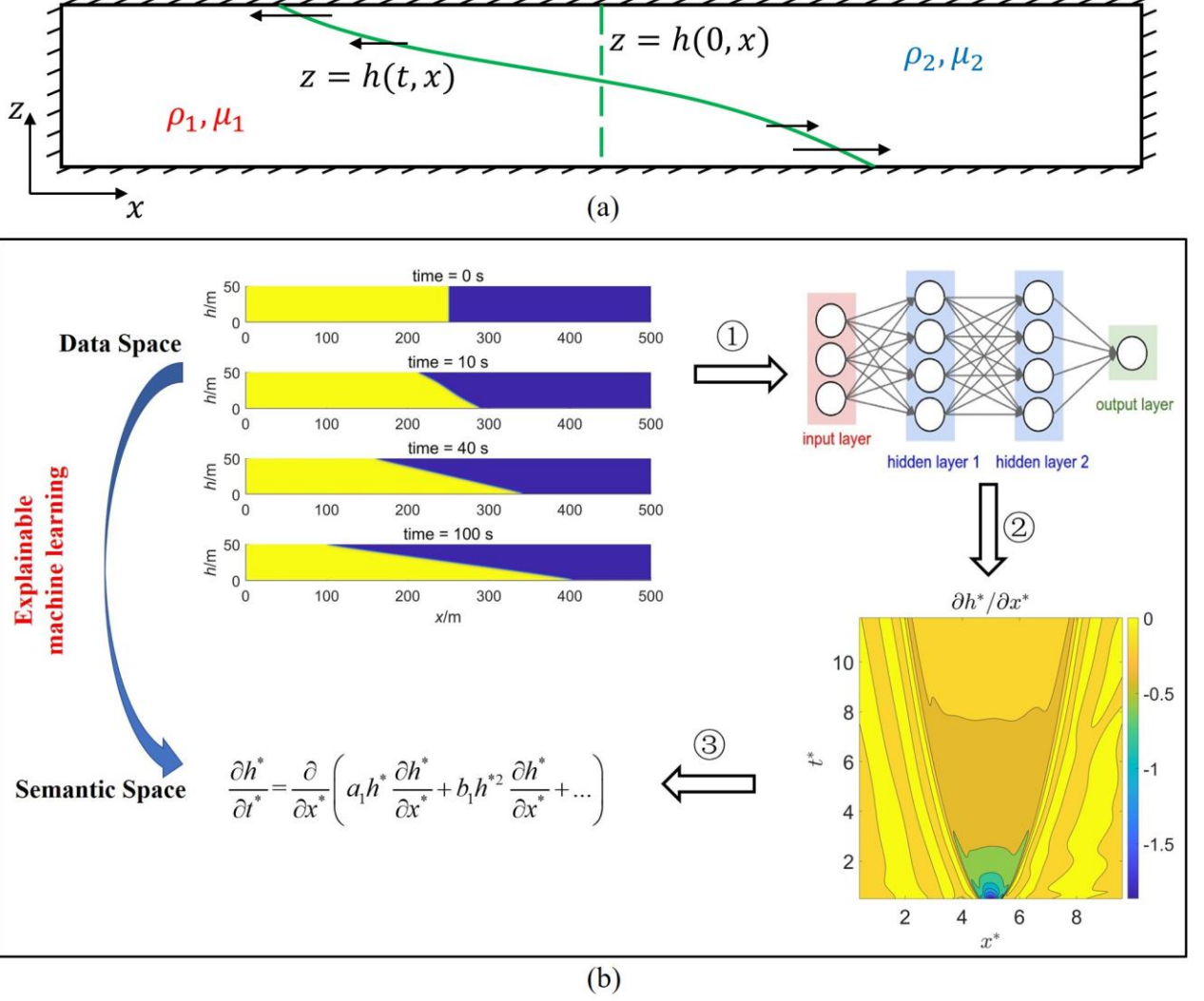


FIG. 1. Illustrations of viscosity gravity currents. (a) Sketch of viscous gravity current in a rectangle vertical fracture. ρ_1 and ρ_2 indicate the density of the two fluids, where $\rho_1 > \rho_2$; and μ_1 and μ_2 indicate the fluid viscosity of the two fluids. The green dashed vertical line indicates the initial interface between the two fluids, and the green solid curve $h(t, x)$ indicates the spatio-temporal evolving current front height. (b) Flowchart of the deep-learning based PDE discovery framework. In order to transform raw simulation data in data space into explainable physical laws (PDEs) in semantic space, the following three steps are necessary. (1) Data reconstruction: training the surrogate based on the deep neural network (DNN); (2) constructing semantic fragments: calculating spatial derivatives and integrated flux; and (3) semantic integration: finding a parsimonious PDE based on sparse regression methods.

Basically, our proposed deep-learning framework for discovering macroscopic PDEs of viscous gravity currents (cf. Figure 1(b)) consists of the following three main steps:

(1) Data reconstruction or surrogate training. In practical scenarios, raw training data can be noisy and randomly distributed in the spatio-temporal domain, which will influence derivative/integral calculations and PDE discovery. Therefore, a deep neural network $NN(t^*, x^*; \theta)$ is first trained by available data to reconstruct the spatio-temporal evolution of front height $h^*(t^*, x^*)$. Theoretically, the neural network can fit any mapping relationship. Compared to other reconstruction methods, neural network based data reconstruction shows good anti-noise and global fitness capability.¹⁰ In addition, the neural network can effectively generate large amounts of meta-data, which is essential for subsequent integral calculation.¹⁸

(2) Semantic fragments construction or derivative/integral calculation. As the neural network based surrogate is built up, derivatives of various orders are calculated by automatic differentiation if a smooth activation function is adopted for neural network training. Moreover, sufficient meta-data are generated on a regular lattice, and numerical integration is accomplished based on conventional approaches, such as Gauss-Legendre quadrature. Within this step, flux F^* , original variable h^* and its various spatial derivatives, such as $\partial h^*/\partial x^*$, $\partial^2 h^*/\partial x^{*2}$ and $\partial^3 h^*/\partial x^{*3}$, can be obtained simultaneously, and these variables are considered as semantic fragments ready for the subsequent step.

(3) Semantic integration or sparse regression. Within this step, the possible semantic fragments are discovered and form the eventual explainable governing equation. Generally, regression methods with parsimony constraints, such as LASSO and genetic algorithm, can be employed to discover the possible PDE terms and corresponding coefficients. Particularly, the genetic algorithm (GA)¹⁸ is adopted in this work. Compared to other sparse regression methods^{9,14,34} that must specify a large number of potential terms and their combinations in the candidate library, the main advantage of GA is that the scale of the candidate library can be much smaller, which is composed of several basic genes, and numerous combinations can be achieved by automatic generation evolution. As a consequence, the GA based deep-learning framework does not need to include the true terms of the underlying equation in the initial candidate library.

First of all, to validate the proposed deep-learning framework for discovering macroscopic PDEs, microscopic simulation data of long-term regimes are first utilized for investigation. Detailed training procedures and parameters are given in the supplemental materials (cf. Supplemental Materials, Section

III). For describing long-term behaviors, the obtained deep-learning based PDEs (DL-PDEs) of the two cases are expressed as follows:

$$\frac{\partial h^*}{\partial t^*} = \frac{\partial}{\partial x^*} \left(0.87226 \cdot h^* \frac{\partial h^*}{\partial x^*} - 0.88138 \cdot h^{*2} \frac{\partial h^*}{\partial x^*} \right) \quad (2)$$

$$\frac{\partial h^*}{\partial t^*} = \frac{\partial}{\partial x^*} \left(0.9875 \cdot h^* \frac{\partial h^*}{\partial x^*} + 0.0325 \cdot h^{*2} \right) \quad (3)$$

Here the GA solution path is discussed to provide insight into how GA works to find the optimized solution. For case I, the discovered best child for flux in the first generation is found to be a set of [1]: $\{h^*, h^{*2}, \partial^2 h^* / \partial x^{*2}\}$, which contains second-order derivative $\partial^2 h^* / \partial x^{*2}$. However, after only three generations, the optimized genomes are converged to [4]: $\{h^* \partial h^* / \partial x^*, h^{*2} \partial h^* / \partial x^*\}$. Quantitatively, the fitness loss eventually decreases to 0.0048 from 0.0077 of the first generation. Most importantly, the initial candidate library, i.e., [0]: $\{h^*, \partial h^* / \partial x^*, \partial^2 h^* / \partial x^{*2}, \partial^3 h^* / \partial x^{*3}\}$, does not need to be complete to include eventual terms in this approach. Indeed, to construct a complete candidate library would usually mean to include an overwhelmingly large number of possible terms, which may greatly increase the computational cost and diminish the performance of sparse regression. It is clear that, to describe the long-term behaviors of viscous gravity currents, the form of flux is highly concise. Since, in each generation, a total of 200 children are generated for evolution, the optimized solution can be determined without much difficulty.

As mentioned previously, one-dimensional macroscopic PDEs of front height for long-term regimes can also be obtained through theoretical analyses.¹⁹ Particularly for the two investigated cases in this work, the theoretical PDEs are expressed as follows(cf. Supplemental Materials, Section IV):

$$\frac{\partial h^*}{\partial t^*} = \frac{\partial}{\partial x^*} \left(h^* \frac{\partial h^*}{\partial x^*} - h^{*2} \frac{\partial h^*}{\partial x^*} \right) \quad (4)$$

$$\frac{\partial h^*}{\partial t^*} = \frac{\partial}{\partial x^*} \left(h^* \frac{\partial h^*}{\partial x^*} \right) \quad (5)$$

It is clear that the trained long-term DL-PDEs (2) and (3) are highly similar to the theoretical results, while coefficients are slightly dissimilar for both cases, and an additional term appears for case II.

Particularly for case I, the corresponding coefficients of dominated terms $h^* \partial h^* / \partial x^*$ and $h^{*2} \partial h^* / \partial x^*$ deviate approximately 12% from the theoretical PDE. For case II, the coefficients of dominated term $h^* \partial h^* / \partial x^*$ deviates approximately only 2% from the theoretical PDE, and coefficient of the additional term is 0.0325, which is also much smaller compared to the dominated term.

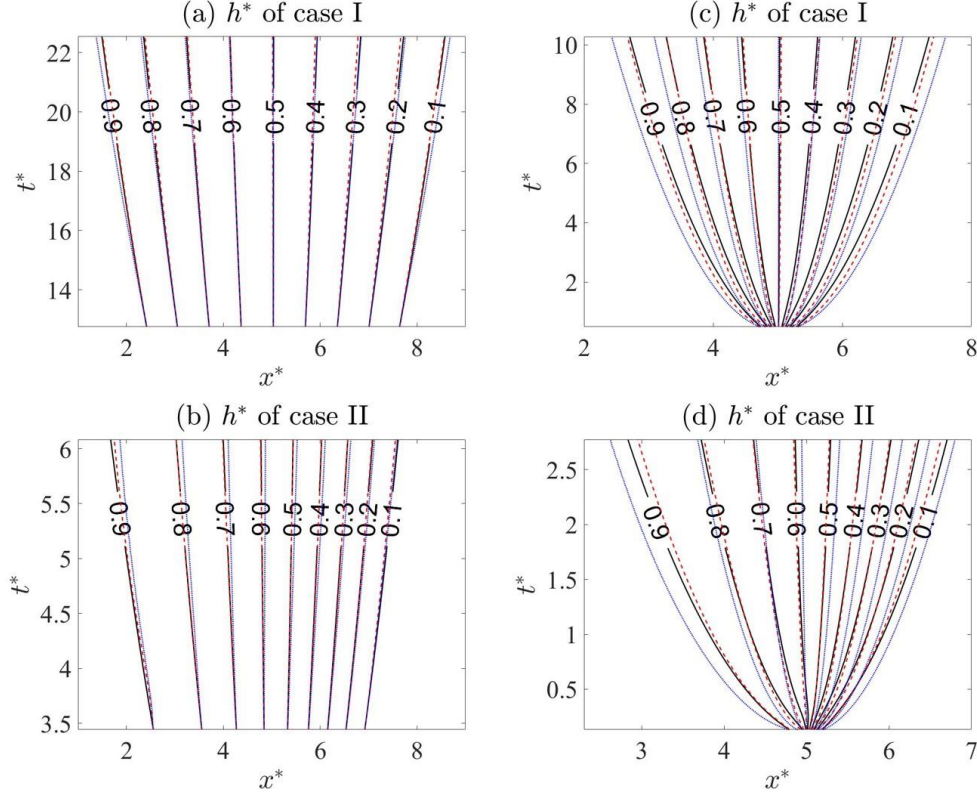


FIG. 2. Contour lines of estimated evolving current front height h^* in posterior tests for two cases: (a) long-term behaviors of case I; (b) long-term behaviors of case II. (c) short-term behaviors of case I; (d) short-term behaviors of case II. The black solid lines are reference values extracted from 2D microscopic simulation results, the long red dashed lines are posterior results of deep-learning based PDEs, and the short blue dashed lines are posterior results of theoretical PDEs. For detailed front height distributions at various times, please refer to the supplemental materials (cf. Supplemental Materials, Section V).

Here, the one-dimensional macroscale equations (2)-(5) are then numerically solved as posterior tests, and the results are illustrated in Figure 2(a) and 2(b). It is clear that the characteristic contour lines of the three data sets are close to each other. Quantitatively, for case I, the total relative errors are estimated as 0.45% and 0.75% for DL-PDE and theoretical PDE, respectively. For case II, the errors are 0.47% and

1.1%, respectively. Therefore, the prediction results of DL-PDEs achieve a superior match with the microscopic simulation results compared to those of theoretical PDEs, irrespective of the training error. This finding implies that modifications are necessary, including smaller coefficients and secondary terms, to better describe viscous gravity currents, even for long-term regimes. More importantly, it is proven that the proposed deep-learning based framework is highly capable and accurate to discover macroscopic equations from raw microscopic simulation data.

Then, the short-term behaviors of viscous gravity currents are investigated. We aim to discover the macroscopic PDEs for describing short-term behaviors, and elucidate the hidden macroscopic mechanisms to identify how deviation between theoretical assumptions and actual situations influences the macroscopic equations. Here, the training parameters of deep-learning are similar to those for long-term DL-PDEs. The eventual learned PDEs for cases I and II are given as follows:

$$\frac{\partial h^*}{\partial t^*} = \frac{\partial}{\partial x^*} \left(a_1 \cdot h^* \frac{\partial h^*}{\partial x^*} + b_1 \cdot h^{*2} \frac{\partial h^*}{\partial x^*} + c_1 \cdot \left(\frac{\partial h^*}{\partial x^*} \right)^2 \right) \quad (6)$$

$$\frac{\partial h^*}{\partial t^*} = \frac{\partial}{\partial x^*} \left(a_2 \cdot h^* \frac{\partial h^*}{\partial x^*} + b_2 \cdot h^* \left(\frac{\partial h^*}{\partial x^*} \right)^2 + c_2 \cdot h^{*4} \frac{\partial h^*}{\partial x^*} \right) \quad (7)$$

where $a_1 = 0.894$; $b_1 = -0.881$; $c_1 = 0.0757$; and $a_2 = 1.006$; $b_2 = 0.215$; $c_2 = -0.571$.

Compared to the DL-PDEs of long-term regimes, it is evident that flux expressions of equations (6) and (7) are more complex, and the GA solution path indicates that many more generations (57 for case I, and 77 for case II) are necessary for convergence (cf. Supplemental Materials, Section VI). Indeed, at the early stage of viscous gravity currents, the fluid field has not yet been fully developed, and theoretical assumptions are too ideal to reflect the actual scenario, implying that a more complex high-dimensional nonlinear mapping relationship is required for describing short-term spatio-temporal evolution of current front height.

By comparing the above deep-learning trained PDEs (DL-PDE) with theoretically derived equations (4) and (5), the following findings are determined:

(1) Flux terms in theoretical PDEs are exactly captured in DL-PDEs, regardless of slightly different coefficients. Particularly for case I, coefficients of $h^* \partial h^* / \partial x^*$ and $h^{*2} \partial h^* / \partial x^*$ are 0.894 and -0.881, while

being 1 and -1 in theoretical PDEs, respectively. Obviously, the characteristic of mutual additive inverse for these two coefficients is not an accidental consequence, but instead reflects the symmetry characteristic of the solution, i.e., $F(h^*, \partial h^* / \partial x^*) = F(1 - h^*, \partial h^* / \partial x^*)$. It is worth noting that this relationship is not satisfied in case II. For case II, the coefficient of leading term $h^* \partial h^* / \partial x^*$ is 1.006, which is very close to the theoretical value of 1.

(2) Excluding the different coefficients of leading terms, it is observed that DL-PDEs provide additional terms for two cases, i.e., $0.0757 \cdot (\partial h^* / \partial x^*)^2$ for case I and $0.215 \cdot h^* (\partial h^* / \partial x^*)^2 - 0.571 \cdot h^{*4} \partial h^* / \partial x^*$ for case II. It should be emphasized that theoretical PDEs are derived for describing long-term behaviors of viscous gravity currents; whereas, in this work, we extend the training data to the whole range, including short-term behaviors. Therefore, we are aimed to find a global solution for viscous gravity currents, which implies that the additional terms in DL-PDEs and modified coefficients of leading terms may be considered as compensation terms for describing short-term range behaviors.

Figure 2(c) and 2(d) illustrates the posterior tests of short-term regimes. It is worth noting that the negative diffusion term in equations (6) and (7) at the early time can dominate the process at the early time, where $-\partial h^* / \partial x^*$ is very large and leads to computation collapse, which is a consequence of the training error tolerance. To solve this issue, necessary artificial viscosity is introduced to counter the negative diffusion under these circumstances (cf. Supplemental Materials, Section VII).

From the characteristic lines of current height in $t - x$ domain, it is inferred that wave structures of current height in the short-term can be considered as rarefaction waves with time-dependent characteristic velocities. The comparison results demonstrate that prediction results of DL-PDEs match the microscopic simulation results better than those of theoretical PDEs. Quantitatively, for case I, the total relative errors are estimated as 1.06% and 2.75% for DL-PDE and theoretical PDE, respectively. For case II, however, the errors are 0.85% and 2.72%, respectively.

As previously mentioned, deviation between reference data and theoretical results is mainly attributed to the assumptions when deriving theoretical PDEs. In theoretical analysis, it is assumed that vertical velocity is zero for the whole domain, while microscopic simulation results infer that this

condition is not fulfilled, particularly near the interface and during the short-term period (cf. Supplemental Materials, Section VIII). As a consequence, the transverse spreading length in $t - x$ domain is larger than ground truth. From the above discussions, the following key points can be inferred for the mechanisms hidden in DL-PDEs:

(1) Smaller coefficients in leading terms for case I weakens the strength of the rarefaction wave and adjusts theoretical PDEs towards ground truth.

(2) Compensation terms for cases I and II essentially represent negative-diffusion mechanisms, which also suppress the over-spreading trend for theoretical PDEs. To explain this, it is necessary to rewrite the compensation terms with first-order derivatives, and we can obtain the dominated second-order derivatives, which indicate diffusion mechanisms (positive or negative). For cases I and II, the compensation diffusion terms are $0.1514 \cdot \partial h^* / \partial x^* (\partial^2 h^* / \partial x^{*2})$ and $0.43 \cdot h^* \partial h^* / \partial x^* (\partial^2 h^* / \partial x^{*2}) - 0.571 \cdot h^{*4} \partial^2 h^* / \partial x^{*2}$, respectively. Moreover, since in this work we have $0 \leq h^* \leq 1$ and $\partial h^* / \partial x^* \leq 0$, the coefficients of the compensation diffusion terms are negative for both cases.

In summary, we proposed a deep-learning framework to elucidate the macroscopic equations of viscous gravity currents based on microscopic simulation data. We show that the proposed deep-learning based PDE discovery framework is essentially an explainable machine learning approach. Microscopic simulation results in data space are eventually transformed into parsimonious PDEs in scientific semantic space through the PDE discovery method. With this framework, explainable compensation terms can be introduced to capture the short-term behaviors. It is found that, in posterior tests, DL-PDEs perform better than the theoretically derived equations. Consequently, the proposed method is demonstrated to be highly beneficial to compensate the drawbacks of theoretical assumptions, construct more accurate governing equations, and deepen our understanding of physical problems. Overall, for a certain physical process, obtained experimental or simulation data contain all kinds of information in data space. However, one needs to extract the most valuable and significant content, and ideally determine intrinsic laws in scientific semantic space. This work demonstrates that the proposed deep-learning based PDE discovery framework constitutes a feasible and efficient approach to solve this problem. In future research, we will extend the framework for learning multi-dimensional equations and for more challenging scenarios.

SUPPLEMENTARY MATERIAL

See the supplementary material for (1) numerical solution of viscous gravity current, (2) effects of changing parameters on evolving history of dimensionless front height, (3) settings for neural network training, (4) theoretical derivation of PDEs for viscous gravity current, (5) detailed spatial distribution of front height in posterior tests, (6) GA solution paths of short-term regimes for two cases, (7) numerical solution and artificial viscosity for deep-learning based PDEs, and (8) insights of fluid velocity field.

DATA AVAILABILITY STATEMENT

The data that support the findings of this study are openly available through Zenodo (<https://doi.org/10.5281/zenodo.4587614>).

References

- ¹ P. Baldi, P. Sadowski, and D. Whiteson, “Searching for exotic particles in high-energy physics with deep learning,” *Nat. Commun.* **5**, 1 (2014).
- ² M. Raissi, A. Yazdani, and G.E. Karniadakis, “Hidden Fluid Mechanics,” *Science* **4741**, 1 (2020).
- ³ C. Kadow, D.M. Hall, and U. Ulbrich, “Artificial intelligence reconstructs missing climate information,” *Nat. Geosci.* **13**, 408 (2020).
- ⁴ M. Reichstein, G. Camps-Valls, B. Stevens, M. Jung, J. Denzler, N. Carvalhais, and Prabhat, “Deep learning and process understanding for data-driven Earth system science,” *Nature* **566**, 195 (2019).
- ⁵ Y. Lecun, Y. Bengio, and G. Hinton, “Deep learning,” *Nature* **521**, 436 (2015).
- ⁶ R. Roscher, B. Bohn, M.F. Duarte, and J. Garcke, “Explainable Machine Learning for Scientific Insights and Discoveries,” *IEEE Access* **8**, 42200 (2020).
- ⁷ H. Xu, H. Chang, and D. Zhang, “DLGA-PDE: Discovery of PDEs with incomplete candidate library via combination of deep learning and genetic algorithm,” *J. Comput. Phys.* **418**, 109584 (2020).

- ⁸ M. Raissi, P. Perdikaris, and G.E. Karniadakis, “Physics-informed neural networks: A deep learning framework for solving forward and inverse problems involving nonlinear partial differential equations,” *J. Comput. Phys.* **378**, 686 (2019).
- ⁹ J. Berg and K. Nyström, “Data-driven discovery of PDEs in complex datasets,” *J. Comput. Phys.* **384**, 239 (2019).
- ¹⁰ H. Xu, H. Chang, and D. Zhang, “DL-PDE: Deep-learning based data-driven discovery of partial differential equations from discrete and noisy data,” *Commun. Comp. Phys.* **29**, 698 (2021).
- ¹¹ S.L. Brunton and J.N. Kutz, “Methods for data-driven multiscale model discovery for materials,” *J. Phys. Mater.* **2**, 044002 (2019).
- ¹² E. Kaiser, J. N. Kutz, and S.L. Brunton, “Sparse identification of nonlinear dynamics for model predictive control in the low-data limit,” *Proc. R. Soc. A Math. Phys. Eng. Sci.* **474**, 2219 (2018).
- ¹³ M. Quade, M. Abel, J. N. Kutz, and S.L. Brunton, “Sparse identification of nonlinear dynamics for rapid model recovery,” *Chaos* **28**, 063116 (2018).
- ¹⁴ S.H. Rudy, S.L. Brunton, J.L. Proctor, and J.N. Kutz, “,” *Sci. Adv.* **3**, e1602614 (2017).
- ¹⁵ S.H. Rudy, A. Alla, S.L. Brunton, and J.N. Kutz, “Data-driven discovery of partial differential equations,” *SIAM J. Appl. Dyn. Syst.* **18**, 643 (2019).
- ¹⁶ S. Zhang and G. Lin, “Robust data-driven discovery of governing physical laws with error bars,” *Proc. R. Soc. A Math. Phys. Eng. Sci.* **474**, 20180305 (2018).
- ¹⁷ M. Maslyaev, A. Hvatov, and A. Kalyuzhnaya, “Data-driven PDE discovery with evolutionary approach,” *arXiv:1903.08011* (2019).

- ¹⁸ H. Xu, D. Zhang, and N. Wang, “Deep learning based discovery of partial differential equations in integral form from sparse and noisy data,” arXiv:2011.11981 (2020).
- ¹⁹ G.H.F. Gardner, J. Downie, and H.A. Kendall, “Gravity segregation of miscible fluids in linear models,” SPE J. **2**, 95 (1964).
- ²⁰ S.H. Davis and L.M. Hocking, “Spreading and imbibition of viscous liquid on a porous base. II,” Phys. Fluids **12**, 1646 (2000).
- ²¹ D. Pritchard, A.W. Woods, and A.J. Hogg, “On the slow draining of a gravity current moving through a layered permeable medium,” J. Fluid Mech. **444**, 23 (2001).
- ²² L. Lake, *Enhanced Oil Recovery* (Prentice Hall, 1988).
- ²³ A.D. Werner, “On the classification of seawater intrusion,” J. Hydrol. **551**, 619 (2017).
- ²⁴ A.D. Werner, M. Bakker, V.E.A. Post, A. Vandenbohede, C. Lu, B. Ataie-Ashtiani, C.T. Simmons, and D.A. Barry, “Seawater intrusion processes, investigation and management: Recent advances and future challenges,” Adv. Water Resour. **51**, 3 (2013).
- ²⁵ A.W. Woods, “Liquid and vapor flow in superheated rock,” Annu. Rev. Fluid Mech. **31**, 171 (1999).
- ²⁶ J. Bear, *Dynamics of Fluids in Porous Media* (Elsevier, 1973).
- ²⁷ D. Pritchard and A.J. Hogg, “Draining viscous gravity currents in a vertical fracture,” J. Fluid Mech. **459**, 207 (2002).
- ²⁸ A.W. Woods and R. Mason, “The dynamics of two-layer gravity-driven flows in permeable rock,” J. Fluid Mech. **421**, 83 (2000).

- ²⁹ V. Di Federico, S. Longo, S.E. King, L. Chiapponi, D. Petrolo, and V. Ciriello, “Gravity-driven flow of Herschel-Bulkley fluid in a fracture and in a 2D porous medium,” *J. Fluid Mech.* **821**, 59 (2017).
- ³⁰ L. Chiapponi, D. Petrolo, A. Lenci, V. Di Federico, and S. Longo, “Dispersion induced by non-Newtonian gravity flow in a layered fracture or formation,” *J. Fluid Mech.* **903**, A14 (2020).
- ³¹ S. Longo, V. Di Federico, and L. Chiapponi, “A dipole solution for power-law gravity currents in porous formations,” *J. Fluid Mech.* **778**, 534 (2015).
- ³² Z. Zheng, I.C. Christov, and H.A. Stone, “Influence of heterogeneity on second-kind self-similar solutions for viscous gravity currents,” *J. Fluid Mech.* **747**, 218 (2014).
- ³³ E. Olsson and G. Kreiss, “A conservative level set method for two phase flow,” *J. Comput. Phys.* **210**, 225 (2005).
- ³⁴ H. Chang and D. Zhang, “Machine learning subsurface flow equations from data,” *Comput. Geosci.* **23**, 895 (2019).

Deep-Learning Discovers Macroscopic Governing Equations for Viscous Gravity Currents from Microscopic Simulation Data

Junsheng Zeng¹, Hao Xu², Yuntian Chen¹, and Dongxiao Zhang^{3*}

¹ Frontier Research Center, Peng Cheng Laboratory, Shenzhen 518000, P. R. China

² College of Engineering, Peking University, Beijing 100871, P. R. China

³ School of Environmental Science and Engineering, Southern University of Science and Technology, Shenzhen 518055, P. R. China

*Corresponding author: Dongxiao Zhang (zhangdx@sustech.edu.cn)

Supplemental Material

I. Numerical solution of viscous gravity current

In this work, refined 2D simulations are performed in order to obtain raw training data for preparation. By substituting Darcy's equation into a continuity equation, a Poisson equation for pressure independent of fluid velocity can be obtained:

$$\nabla^2 P = \frac{g\mu}{k} \frac{\partial \rho}{\partial z} \quad (\text{S.1})$$

where k is the permeability of fracture; ρ and μ are the fluid viscosity and density, respectively; P is the pressure gradient; \vec{g} is the gravity acceleration; and z indicates the vertical direction.

The pressure equation is numerically discretized with the center difference scheme. Finally, a cinque-diagonal linear system is obtained, and the AGMG solver based on the multi-grid technique¹ is adopted to solve the linear system.

In viscous gravity current, two phases of fluid exist, i.e., heavy fluid and light fluid. Therefore, the interface tracking method is necessary in order to capture the interface between the two phases and

maintain the sharpness of front under the Eulerian framework. A conservative level set method² is applied to solve this issue. In this method, the level set function is evolved in the following two steps:

$$\frac{\partial C}{\partial t} + \frac{1}{\phi} \nabla \cdot (C \vec{u}) = 0 \quad (\text{S.2})$$

$$\frac{\partial C}{\partial \tau} + \nabla \cdot \left[C(1-C) \frac{\nabla C}{\|\nabla C\|} \right] = \varepsilon \Delta C \quad (\text{S.3})$$

where C is the level set function or color function; \vec{u} is the two-dimensional velocity of fluid; ϕ is the porosity; τ is the artificial time; and ε is the artificial viscosity. Note that equation (S.2) has been written in a conservative form by utilizing the continuity equation (S.3), and the artificial viscosity ε is introduced in consideration of numerical stability. The above equations indicate the advection step and the artificial compression step, respectively.

For the advection step, the third-order Runge-Kutta TVD scheme³ and fifth-order WENO scheme^{4,5} are applied for temporal and spatial discretizations, respectively. For the artificial compression step, a center difference scheme is adopted, and after several artificial time steps, the color function converges to maintain a constant interface width.

For each time step, fluid pressure and velocity are first determined by solving the pressure equation, and color function C is then updated according to equation (S.2) and (S.3). Pressure calculation and evolution of color function are sequentially solved through the simulation timeline.

II. Effects of changing parameters on evolving history of dimensionless front height

Three more tests of different parameters are simulated to investigate the effects, and the parameter settings are shown in Table S.1. Key parameters include domain height, density difference, fracture width (related to permeability), and fluid viscosity.

Table S.1. Physical parameter settings of four tests for two cases.

	Test I	Test II	Test III	Test IV
Domain height H (m)	50	25	100	10

Density difference $\Delta\rho$ (kg/m^3)	0.3	0.1	0.02	0.2
Fracture width w (m)	0.005	0.005	0.002	0.001
Fluid viscosity μ_1 (Pa·s) of case I and case II	0.001 and 0.04	0.001 and 0.04	0.01 and 0.4	0.1 and 4

Figure S.1 illustrates the evolving dimensionless front height for the above tests. It is clear that for both case I and case II, the contour lines of the corresponding four tests match each other well, and the relative error is less than 0.1%, which is mainly due to accumulation of numerical error. Therefore, through numerical experiments it is proven that once the dimensionless group as listed in equation (1) is utilized, evolving histories of dimensionless front height are all the same, regardless of changing dimensional parameters. Moreover, the obtained DL-PDEs can represent universal laws for similar processes if the dimensionless data are utilized for subsequent deep-learning.

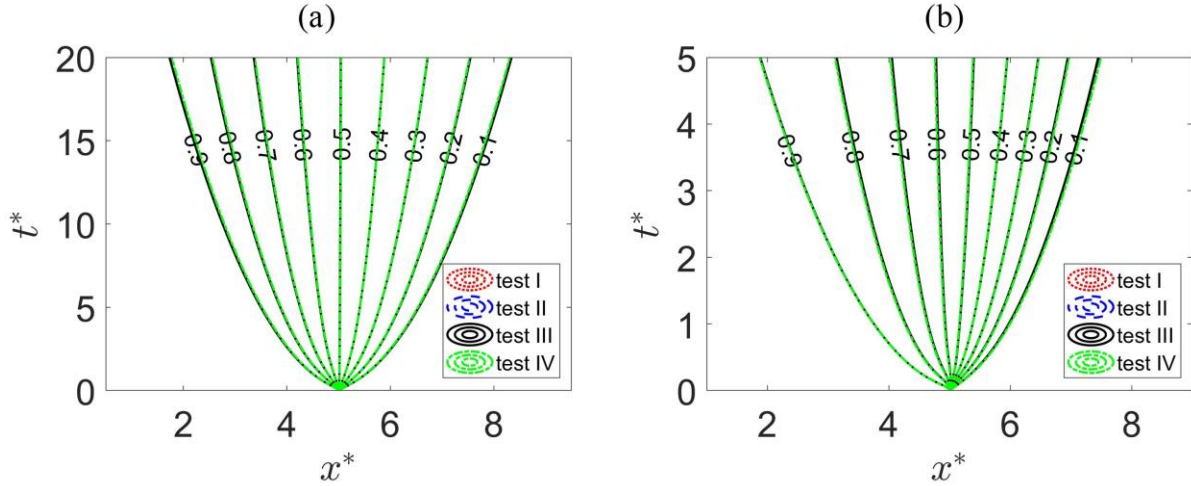


Figure S.1. Contour lines of dimensionless front height in different tests: (a) four tests of case I; (b) four tests of case II. Total contour lines of nine contour levels are illustrated: 0.1, 0.2, ..., 0.9.

III. Settings for neural network training

Training details and parameter settings utilized in this work during the three steps are listed as follows:

(1) For the data reconstruction step, a five-layer fully-connected neural network with 100 neurons per layer, and soft-plus activation function are used for training. For each case, a total of 80% of 500×500 spatial-temporal points are chosen as training data. After training approximately 100,000 epochs, the mean square error (MSE) between raw data and prediction results decreases to a minimal level of 10^{-7} , which is considered to be sufficiently converged.

(2) For derivative/integration calculation, 300×300 lattice points of the inner spatial-temporal domain are selected, and a five-point Gauss-Legendre quadrature scheme is adopted here to calculate flux. In order to improve the regression performance, a large amount of trivial samples out of the mentioned 90,000 lattice points, e.g., $h^* \approx 1$ and $h^* \approx 0$, need to be omitted because flux is also trivial in these regions, i.e., $F^* \approx 0$.

(3) For the sparse regression step, four basic genes are chosen as the candidate library, i.e., $(h^*, \partial h^* / \partial x^*, \partial^2 h^* / \partial x^{*2}, \partial^3 h^* / \partial x^{*3})$. Population size is set as 200 per generation, and genes are randomly combined with each other as the initial generation. Mutation rate and cross-over rate are set as 20% and 80%, respectively. Fitness function is defined as $Fitness = -\sum |F_{ref}^* - F_{ga}^*| / N - \lambda \sum a_i / |a_i|$, where N is the number of sample data; and a_i is the coefficient of the i -th derivative combination. The first term indicates data fitness between reference flux value F_{ref}^* and estimated value F_{ga}^* , and the last term indicates the parsimony constraint, i.e., the total number of terms, which is controlled by hyper parameter λ . In this work, λ is set as 0.002 for most cases.

IV. Theoretical derivation of PDEs for viscous gravity current

We now briefly review derivation details regarding theoretical PDEs (4) and (5), which describe the long-term asymptotic behaviors of current front height. Consider the viscous gravity current process as illustrated in Figure S.2. Assume that vertical flow is sufficiently smaller than horizontal flow, i.e., $u_z \ll k\rho g / \mu$, where u_z indicates the vertical component of fluid velocity. Under this condition, the pressure and velocity distribution can be analytically obtained.

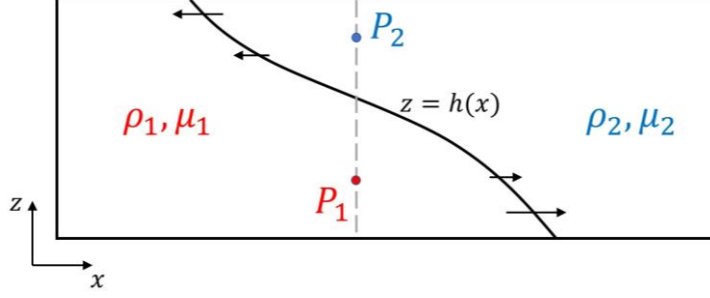


Figure S.2. Illustration of viscous gravity current height in a vertical fracture. Quantities of heavy and light fluid are marked as red and blue color, respectively.

The following derivation follows Gardner et al.'s work⁶. Under the assumption of zero vertical velocity, the pressure gradient in the vertical direction can be simplified as $\partial P / \partial z = -\rho g$. Pressure across the vertical lines of the two phases can then be analytically expressed as:

$$P_2 = \pi + \rho_2 g (H - z), \quad z > h(x) \quad (\text{S.4})$$

$$P_1 = \pi + \rho_2 g (H - h) + \rho_1 g (h - z), \quad z > h(x) \quad (\text{S.5})$$

where P_1 and P_2 indicate fluid pressure, as illustrated in Figure S.2; $h(x)$ indicates the horizontally varying current front height; H is the total domain height; and π is the reference pressure in the horizontal direction.

Then, the horizontal velocity for the two phases can be written as follows:

$$u_{x,2} = -\frac{k}{\mu_2} \frac{\partial \pi}{\partial x} \quad (\text{S.6})$$

$$u_{x,1} = -\frac{k}{\mu_1} \left(\frac{\partial \pi}{\partial x} + \Delta \rho g \frac{\partial h}{\partial x} \right) \quad (\text{S.7})$$

In a domain with a closed boundary, it is fulfilled along any vertical line that:

$$\int_0^H u_x dz = u_{x,1} h + u_{x,2} (H - h) = 0 \quad (\text{S.8})$$

By combining equations (S.6)-(S.8), it is trivial to obtain the following formula:

$$u_{x,1} = k \Delta \rho g \frac{\partial h}{\partial x} \bigg/ \left(\mu_1 + \mu_2 \frac{h}{H-h} \right) \quad (\text{S.9})$$

For phase 1, we also have the continuity equation:

$$\frac{\partial h}{\partial t} + \frac{\partial(u_{x,1} h)}{\partial x} = 0 \quad (\text{S.10})$$

By substituting equation (S.9) into (S.10), the PDE of current height can finally be determined:

$$\frac{\partial h}{\partial t} - k \Delta \rho g \frac{\partial}{\partial x} \left(\frac{h(H-h)}{\mu_1(H-h) + \mu_2 h} \frac{\partial h}{\partial x} \right) = 0 \quad (\text{S.11})$$

Consider the two cases in this work, i.e., $\mu_1 = \mu_2$ and $\mu_1 \gg \mu_2$. The above equation can then be further simplified as:

$$\frac{\partial h}{\partial t} - \frac{k \Delta \rho g}{\mu_1 H} \frac{\partial}{\partial x} \left(h(H-h) \frac{\partial h}{\partial x} \right) = 0 \quad (\text{S.12})$$

$$\frac{\partial h}{\partial t} - \frac{k \Delta \rho g}{\mu_1} \frac{\partial}{\partial x} \left(h \frac{\partial h}{\partial x} \right) = 0 \quad (\text{S.13})$$

which correspond to equations (4) and (5) in dimensionless form, respectively.

Note that in this work, two regimes are investigated for both cases, i.e., long-term and short-term regimes. In general, long-term regimes imply that nondimensional vertical velocity is sufficiently small, i.e., $u_z^* = u_z \mu_1 / (\Delta \rho g k) \ll 1$. Here, we distinguish these two regimes through another more intuitive indicator, i.e., the dimensionless horizontal spanning distance $\Delta x^* = \|x|_{h^* \rightarrow 0} - x|_{h^* \rightarrow 1}\|$ of the current front interface. The long-term regime is defined as $\Delta x^* > 6$, and the short-term regime as $0 \leq \Delta x^* \leq 6$. Under this condition, for both cases, the calculated average nondimensional vertical velocities of long-term regimes are less than 0.05, which is acceptably small. Furthermore, for subsequential deep-learning, the amount of training data (spatio-temporal points of front height) of the two regimes is set as the same size.

V. Detailed spatial distribution of front height in posterior tests

The spatial distribution of dimensionless front height at different times is illustrated in Figures S.3-S.6. In all figures, black solid lines are reference values extracted from 2D microscopic simulation results, long red dashed lines are posterior results of deep-learning based PDEs, and short blue dashed lines are posterior results of theoretical PDEs.

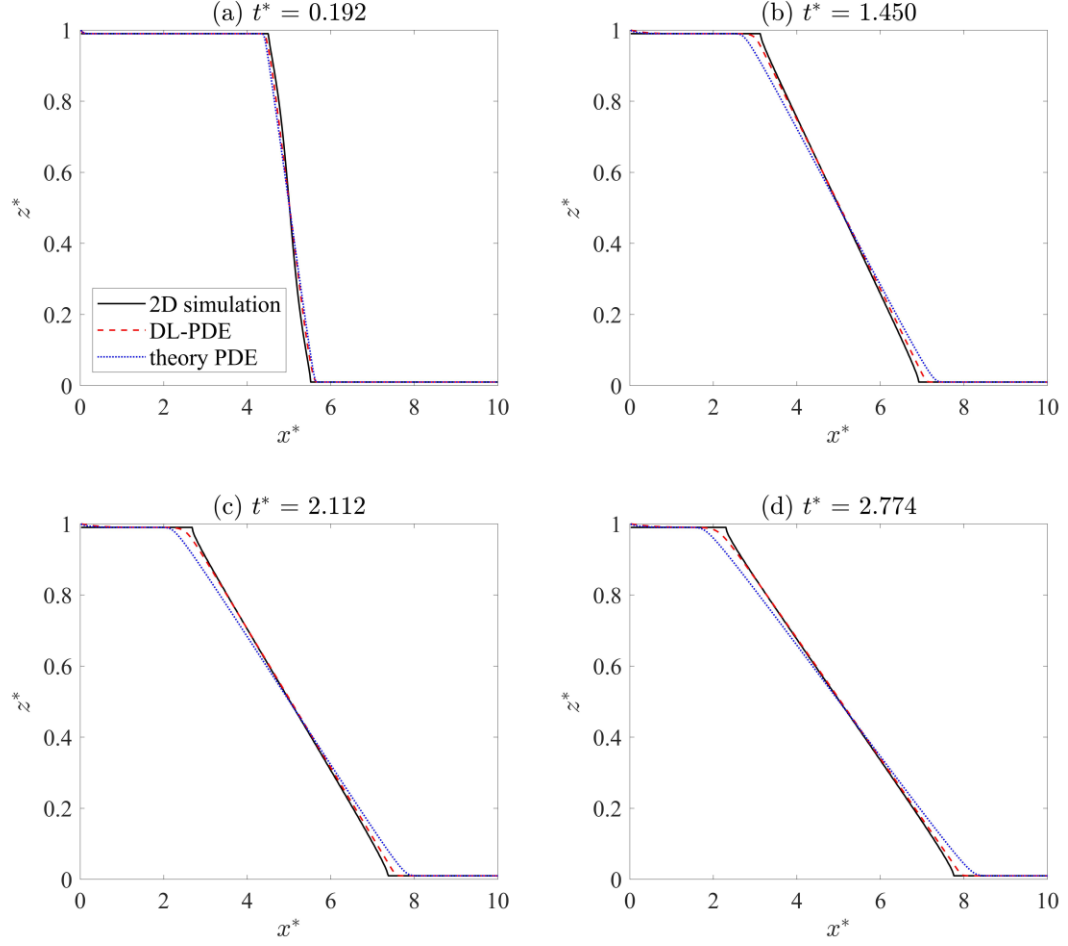


Figure S.3. Short-term behaviors of case I.

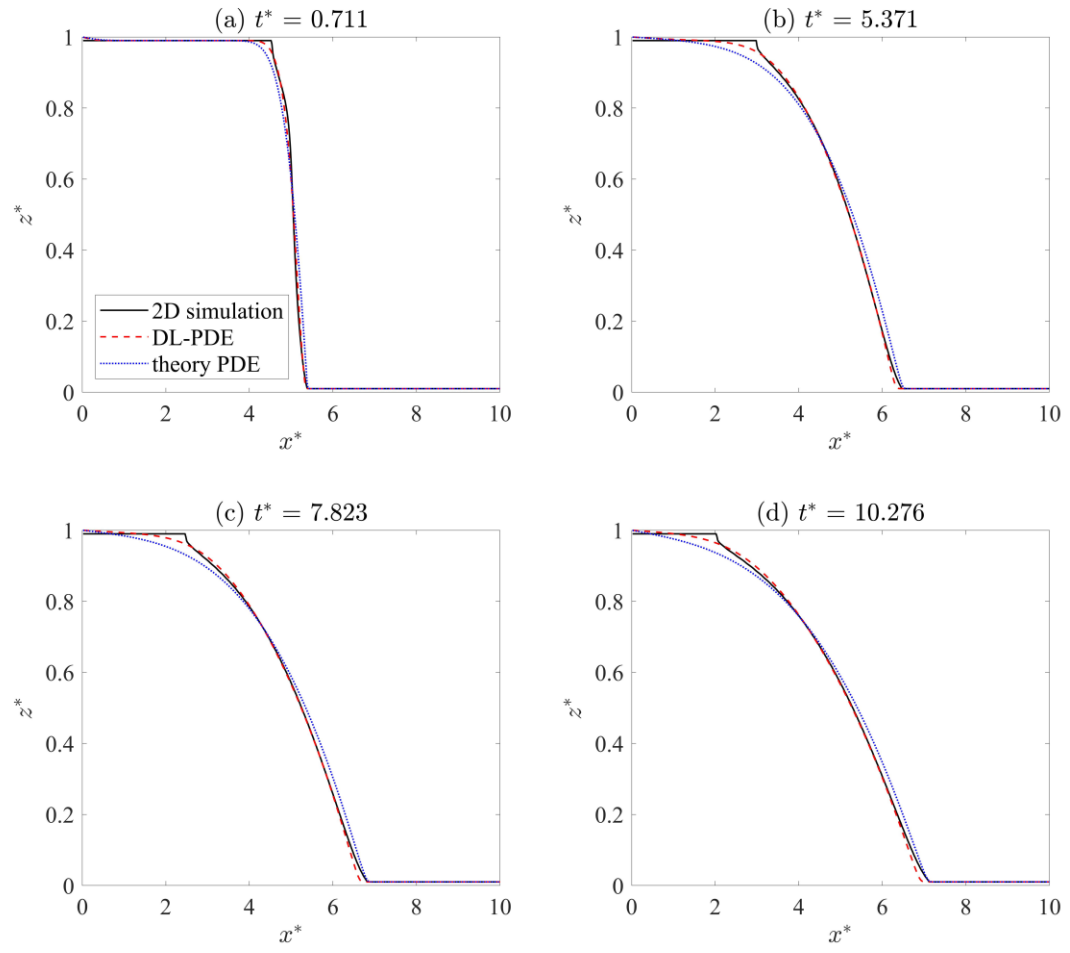


Figure S.4. Short-term behaviors of case II.

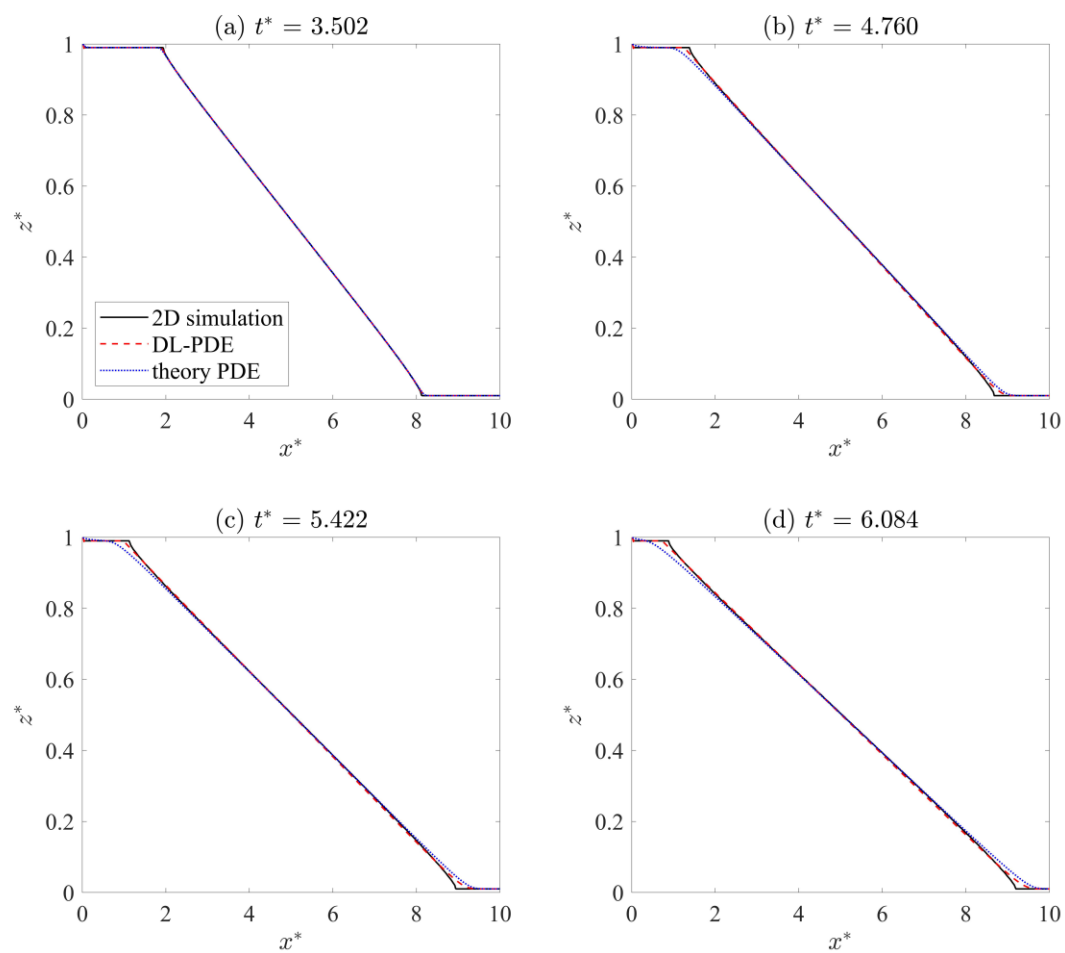


Figure S.5. Long-term behaviors of case I.

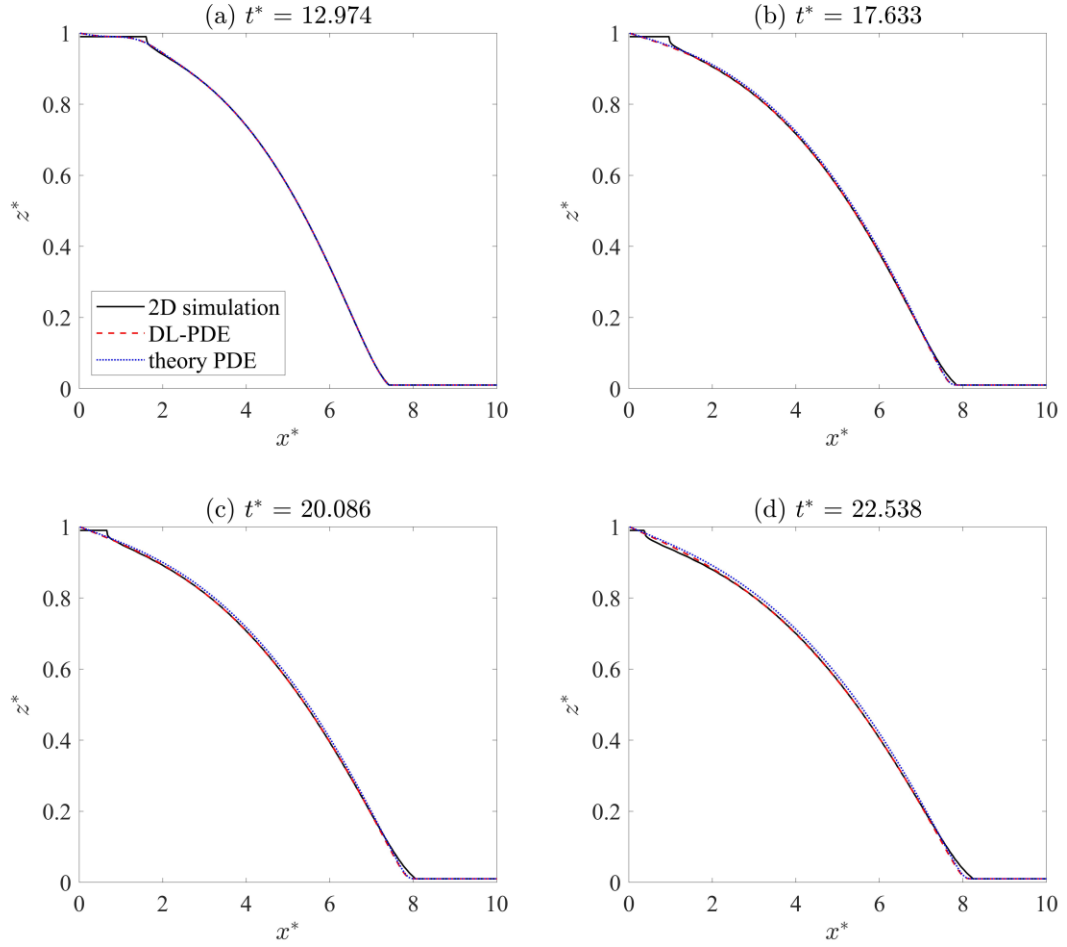


Figure S.6. Long-term behaviors of case II.

VI. GA solution paths of short-term regimes for two cases

Table S.2 and S.3 list the solution paths of short-term regimes for the two cases. For the first generation of case I, the best child for flux is found to be a single term of $\partial h^* / \partial x^*$, which indicates a pure diffusion mechanism. The fitness error of the first generation is approximately 0.014, which indicates that there is room for further improvement. It is clear that, through genome mutations and cross-over manipulations within several generations, increasingly complex terms are discovered and replace subordinate terms. Finally, the solution is converged in the 57th generation, in which fitness error is approximately 0.007, which corresponds to equation (6). On the other hand, the solution path of case II

exhibits a contrasting evolution direction when finding the optimized solution. The best child in the first generation is composed of five complex terms, including second-order and third-order gradients. However, during generation evolution, these terms are somehow replaced and eliminated. Although there is no dramatic decrease in fitness error, which changes from 0.0195 to 0.0133, the final discovered PDE form is more concise than the first generation. It is clearly shown that the initial candidate library does not need to be complete in this approach. Indeed, to construct a complete candidate library would mean to include an overwhelmingly large number of possible terms.

Table S.2. GA solution path of case I.

Generations	Structure of discovered best child
1	$\frac{\partial h^*}{\partial x^*}$
2	$h^*, \frac{\partial h^*}{\partial x^*}, h^{*2}$
3	$h^{*2} \left(\frac{\partial h^*}{\partial x^*} \right)^3, h^* \frac{\partial h^*}{\partial x^*}, h^{*2} \frac{\partial h^*}{\partial x^*}$
20	$h^* \frac{\partial h^*}{\partial x^*}, h^{*2} \frac{\partial h^*}{\partial x^*}$
57	$h^* \frac{\partial h^*}{\partial x^*}, h^{*2} \frac{\partial h^*}{\partial x^*}, \left(\frac{\partial h^*}{\partial x^*} \right)^2$
100	$h^* \frac{\partial h^*}{\partial x^*}, h^{*2} \frac{\partial h^*}{\partial x^*}, \left(\frac{\partial h^*}{\partial x^*} \right)^2$

Table S.3. GA solution path of case II.

Generations	Structure of discovered best child
1	$h^*, h^* \frac{\partial^2 h^*}{\partial x^{*2}} \frac{\partial^3 h^*}{\partial x^{*3}}, h^{*2}, h^* \frac{\partial h^*}{\partial x^*}, \left(\frac{\partial h^*}{\partial x^*} \right)^2$
3	$\frac{\partial^3 h^*}{\partial x^{*3}}, h^*, h^* \frac{\partial h^*}{\partial x^*}, h^{*3}$
4	$h^*, h^* \frac{\partial h^*}{\partial x^*}, h^{*2}$
6	$h^*, h^* \frac{\partial h^*}{\partial x^*}, h^{*2}, h^{*2} \left(\frac{\partial h^*}{\partial x^*} \right)^2$
18	$h^{*3} \frac{\partial h^*}{\partial x^*}, h^* \frac{\partial h^*}{\partial x^*}, h^* \left(\frac{\partial h^*}{\partial x^*} \right)^2$
77	$h^* \frac{\partial h^*}{\partial x^*}, h^* \left(\frac{\partial h^*}{\partial x^*} \right)^2, h^{*4} \frac{\partial h^*}{\partial x^*}$
100	$h^* \frac{\partial h^*}{\partial x^*}, h^* \left(\frac{\partial h^*}{\partial x^*} \right)^2, h^{*4} \frac{\partial h^*}{\partial x^*}$

VII. Numerical solution and artificial viscosity for deep-learning based PDEs

In posterior tests, the obtained 1D PDE is numerically solved, and the results are compared with the raw data extracted from refined 2D simulations. To obtain a numerical solution for deep-learning based PDEs, the center difference scheme is first applied for calculating the flux in the cell center, and then the WENO scheme is utilized for flux reconstruction similar to solving equation (S.2).

However, it is not guaranteed that the deep-learning based PDEs are exactly numerically stable because of training error. To illustrate this, let us take equation (6) as an example. Equation (6) can be rewritten as follows:

$$\frac{\partial h^*}{\partial t^*} = \left(a_1 + 2b_1 h^*\right) \frac{\partial h^*}{\partial x^*} \frac{\partial h^*}{\partial x^*} + \left(a_1 h^* + b_1 h^{*2} + 2c_1 \frac{\partial h^*}{\partial x^*}\right) \frac{\partial^2 h^*}{\partial x^{*2}} \quad (\text{S.14})$$

The two terms on the right-hand side of equation (S.14) can be regarded as parametric convection and diffusion terms, respectively. In this case, if the coefficient of diffusion term is positive, i.e., $a_1 h^* + b_1 h^{*2} + 2c_1 \partial h^* / \partial x^* > 0$, then the system is numerically stable. If the coefficient is negative, however, the system will break down due to anti-diffusion. According to our numerical experiments, it is found that the system is more likely to collapse where $-\partial h^* / \partial x^*$ is very large, which corresponds to the early time in the viscous gravity current.

To suppress the non-physical anti-diffusion terms, artificial viscosity η is introduced for deep-learning based PDEs when needed, which is written as:

$$\frac{\partial h^*}{\partial t^*} - \frac{\partial}{\partial x^*} \left(a_1 \cdot h^* \frac{\partial h^*}{\partial x^*} + b_1 \cdot h^{*2} \frac{\partial h^*}{\partial x^*} + c_1 \cdot \left(\frac{\partial h^*}{\partial x^*} \right)^2 \right) = \eta \frac{\partial^2 h^*}{\partial x^{*2}} \quad (\text{S.15})$$

where $\eta = -\min\left(0, a_1 h^* + b_1 h^{*2} + 2c_1 \partial h^* / \partial x^*\right)$. Similar remedies are adopted for other DL-PDEs when needed during posterior tests, such as in equation (7).

VIII. Insights of fluid velocity field

It is seen from Figure S.7 that, over the whole simulation period, the absolute relative magnitude of vertical velocity ranges markedly from 0.5 to 1. Moreover, the vertical velocity is fairly comparable to the horizontal velocity, which is particularly significant near two interface tails. Therefore, the assumption of zero vertical velocity is not valid, and theoretical PDEs cannot precisely reproduce the evolving process of viscous gravity current. Furthermore, modified coefficients and compensation terms are necessary to be introduced for improvement.

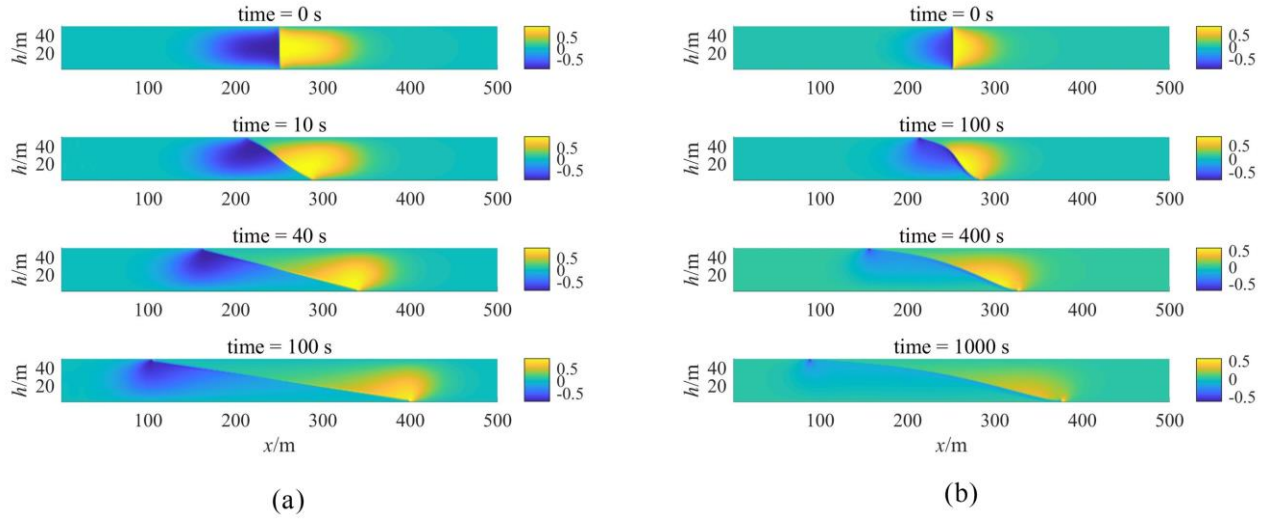


Figure S.7. Contour of relative magnitude of vertical velocity component $u_z / \sqrt{u_x^2 + u_z^2}$ at various time instances for two cases: (a) case I; (b) case II.

References

- ¹ Yvan Notay, Electron, “An aggregation-based algebraic multigrid method,” *Trans. Numer. Anal.* **37**, 123 (2010).
- ² E. Olsson and G. Kreiss, “A conservative level set method for two phase flow,” *J. Comput. Phys.* **210**, 225 (2005).
- ³ S. Gottlieb and C.W. Shu, “Total variation diminishing Runge-Kutta schemes,” *Math. Comput. Am. Math. Soc.* **67**, 73 (1998).
- ⁴ M. Roostaei, A. Nouri, V. Fattahpour, and D. Chan, “Numerical simulation of proppant transport in hydraulic fractures,” *J. Pet. Sci. Eng.* **163**, 119 (2018).
- ⁵ G.S. Jiang and C.W. Shu, “Efficient implementation of weighted ENO schemes,” *J. Comput. Phys.* **126**, 202 (1996).

⁶ G.H.F. Gardner, J. Downie, and H.A. Kendall, “Gravity segregation of miscible fluids in linear models,” SPE J. **2**, 95 (1964).